Effect of the MJO on East Asian Winter Rainfall as Revealed by an SVD Analysis

YUN-LAN CHEN,[a,b] CHUNG-HSIUNG SUI,[b] CHIH-PEI CHANG,[b,c] AND KAI-CHIH TSENG[d,e]

[a] *Central Weather Bureau, Taipei, Taiwan*
[b] *Department of Atmospheric Sciences, National Taiwan University, Taipei, Taiwan*
[c] *Department of Meteorology, Naval Postgraduate School, Monterey, California*
[d] *Program in Atmospheric and Oceanic Science, Princeton University, Princeton, New Jersey*
[e] *NOAA/Geophysical Fluid Dynamics Laboratory, Princeton, New Jersey*

(Manuscript received 9 December 2020, in final form 7 August 2021)

ABSTRACT: This paper studies the influences of the Madden–Julian oscillation (MJO) on East Asian (EA) winter rainfall using the singular value decomposition (SVD) approach. This method uses two-dimensional instead of latitudinally averaged variables in the commonly used real-time multivariate MJO (RMM) index. A comparison of the two approaches is made using the same OLR and zonal wind data over 37 boreal winter seasons of December–March. The SVD composite reveals a more conspicuous and coherent variation throughout the MJO cycle, while the RMM composite is more ambiguous. In particular, the SVD analysis identifies the convection anomalies over the Maritime Continent and the subtropical western Pacific (MCWP) as a major cause of enhanced rainfall in EA at RMM phases 8 and 1. This is at least one-eighth of a cycle earlier than the phases of convection development over the Indian Ocean (IO) that were emphasized by previous studies. A linearized global baroclinic model is used to demonstrate the mechanism of MJO forcing on EA rainfall during various phases, with a focus on the MCWP cooling. The result shows that the anomalous MCWP cooling and the resultant low-level anticyclonic flow interact with the East Asian jet, leading to an overall weakened EA winter monsoon circulation. The associated anomalous overturning circulation, with ascending motion and low-level horizontal moisture convergence in EA, contributes to the enhanced rainfall. This model result supports the interpretation of the SVD analysis, in that the MCWP cooling induced anomalous meridional circulation is a more direct cause of enhanced EA rainfall than the IO heating (or the IO–MCWP heating dipole) induced Rossby wave teleconnection.

KEYWORDS: Madden-Julian oscillation; Waves, atmospheric; Rainfall

1. Introduction

The Madden–Julian oscillation (MJO) accounts for a large portion of the tropical precipitation and global circulation variability in the troposphere. Matthews et al. (2004) estimated that the MJO contributes up to 70% of variance of the 200-hPa circulation in the tropics and 35%–40% in the Northern Hemispheric extratropics (less than 20% in the Southern Hemispheric extratropics). Its dominance in the tropics made it useful for synoptic to intraseasonal forecasts in many tropical regions. Its influences on extratropical weather have also attracted strong interest and have been studied extensively for both theoretical understanding and applications, particularly on extended-range weather forecasts.

The MJO is associated with strong variation of tropical deep convection, and therefore its influence on extratropical weather can be formulated as a problem to study forcing by tropical heat source on the extratropical atmosphere. Earlier studies used barotropic and baroclinic models to show extratropical responses to tropical heating as a Rossby wave train propagating out of the tropics in the upper troposphere (e.g., Hoskins and Karoly 1981; Jin and Hoskins 1995). Ferranti et al. (1990) studied tropical–extratropical interaction associated with the 30–60-day oscillation and its impact on medium- and extended-range prediction. The anomalous upper-tropospheric divergence associated with tropical heating acts as a Rossby wave source for poleward dispersing extratropical wave activity (Sardeshmukh and Hoskins 1988). Hoskins and Ambrizzi (1993) suggested the possible existence of waveguides in the Asian, North Atlantic, and Southern Hemispheric jets. The generation of barotropic Rossby waves by tropical heating in the presence of vertical shear of mean flow, which allows the waves to propagate to extratropics, has been discussed by Lim and Chang (1986), Wang and Xie (1996) and Xie and Wang (1996).

More recent studies used primitive equation models to perform numerical experiments subject to the MJO-like forcing, which typically is represented by a monopole, dipole, or

Corresponding author: Chung-Hsiung Sui, sui@as.ntu.edu.tw

DOI: 10.1175/JCLI-D-20-0941.1

tripole heating structure (e.g., Matthews et al. 2004; Seo and Son 2012; Seo and Lee 2017). The MJO heating has the largest amplitude in the eastern Indian Ocean–western Pacific region during boreal winter. Significant extratropical responses have been found in the downstream Pacific jet region (Pacific, North America, and Atlantic) to the MJO heating (e.g., Mori and Watanabe 2008; Lin et al. 2009; Tseng et al. 2018).

The proximity to the Pacific jet regions makes East Asia (EA) a particularly interesting region to analyze the MJO influences on its wintertime weather. Jeong et al. (2005, 2008) studied the simultaneous relationship between the MJO and wintertime surface air temperature (SAT) and precipitation in East Asia. Using the real-time multivariate MJO (RMM) index (Wheeler and Hendon 2004) that divides the MJO into eight phases and the corresponding location of maximum convection, they suggested that the MJO–EA precipitation relation is accompanied by the strong vertical motion anomalies near the entrance region of the East Asian upper tropospheric jet. The vertical motion anomalies are accounted for mostly by the quasigeostrophic forcing of the MJO during RMM phases 2–3 that can be diagnosed in a generalized omega equation following Kim et al. (2006).

He et al. (2011) observed a relation between a single tropical convection center (their EOF1 mode of OLR) over the Maritime Continent (90°–150°E), and large areas of cold anomalies with reduced precipitation in the EA region north of 20°N. This relation is evident from the peak EOF1 phase and the following two pentads. They also used a linearized global primitive equation model to simulate the East Asian SAT and precipitation as a response to the tropical MJO diabatic heating. This response is related to the local Hadley cell and the circulation anomaly of the Northern Hemisphere branch of the equatorially trapped Rossby wave.

Studies by Jia et al. (2011), Hung et al. (2014), and Liu and Hsu (2019) confirmed the findings of a correspondence between MJO convection over the Indian Ocean and East Asian rainfall. In these studies, rainfall was observed to increase in southeast China and Taiwan corresponds to the MJO RMM phases 2–4, and to decrease in RMM phases 6–8 when the Maritime Continent is under suppressed condition. The increased rainfall was generally attributed to the MJO-generated extratropical Rossby wave train that can induce northward moisture transport originated from the Bay of Bengal and the South China Sea. [See a recent review of the MJO influence on East Asia by Li et al. (2020)].

The relationship between the MJO active phases over the eastern Indian Ocean and Maritime Continent and wintertime EA rainfall found by the above investigators suggests the potential of using MJO to guide rainfall forecast at synoptic or longer lead times. For example, Li et al. (2016) developed a model for extended-range forecasting of spring rainfall in southern China by using the MJO index. To assess the degree of the usefulness of this potential, we stratify the December–March (DJFM) days during MJO RMM phases 2–3 into three groups of equal number of days (cases) according to the order of EA rainfall anomalies, and performed composites of 850-hPa wind and rainfall fields for each of the three groups. The

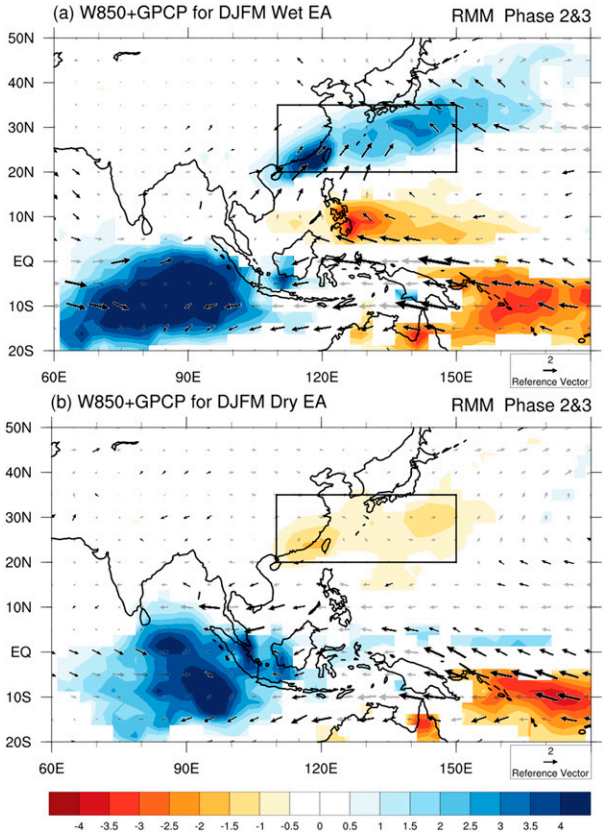

FIG. 1. Composites of anomalous GPCP rainfall (mm day^{-1}) and 850-hPa wind (m s^{-1}) for the (a) top 1/3 and (b) bottom 1/3 of days in RMM phases 2 and 3 arranged by the frequency distribution of averaged GPCP rainfall anomalies in East Asian rainfall region (black rectangle). Rainfall anomalies with statistical significance [95% confidence interval (CI)] are shaded. Wind anomalies with statistical significance are shown in dark wind vectors; the rest are shown in gray. The climatological rainfall amount for East Asian rainfall region is 2.6 mm day^{-1}.

anomalies are computed from long-term mean DJFM with the seasonal cycle removed (described in section 2). Figure 1 shows the composites of the top one-third and the bottom one-third groups, respectively. The top one-third group with an organized large positive EA rainfall anomaly pattern indeed corresponds to strong MJO rainfall anomalies in phases 2–3. However, the MJO signal is also quite conspicuous in the bottom one-third group in which the average EA rainfall anomalies are negative and also well organized. This result indicates that the MJO–EA rainfall relationship is far from ideal, and significant uncertainty exists in using the MJO RMM phases for rainfall forecasting.

Most of the observational studies used either 1) the RMM index that is constructed from the outgoing longwave radiation (OLR) and zonal winds at 850 and 200 hPa averaged over the equatorial belt between 15°S and 15°N or 2) the tropical OLR field directly to represent the MJO. The RMM is one-dimensional, and the tropical OLR is also close to being a one-dimensional index because it is principally an east–west elongated field with little signal outside of the tropical belt.

Thus, it also does not contain much information on the meridional structure of the basic fields. In a study of East Asian winter monsoon cold surges, Chang et al. (2005) used a singular value decomposition (SVD) of OLR and the low-level meridional wind field to analyze the interaction between the MJO and cold surges. It turned out that the meridional structure of the wind field in the subtropics was crucial in elucidating the negative impact of the MJO on the cold surges in the South China Sea. This information that is revealed in the two-dimensional SVD analysis was lost when the one-dimensional RMM scheme is used to represent the MJO.

Since the MJO influences EA wintertime rainfall through a process of meridional interaction, we will use the SVD method to resolve the MJO phase structure. The purpose of this paper is to find out if a two-dimensional analysis, such as the SVD that better defines the MJO structure, will reveal important mechanisms of the MJO influences on wintertime East Asian rainfall that were obscured in previous studies using the RMM scheme. We will also use a linear baroclinic model to examine and verify the mechanism revealed by the observational study. Section 2 describes the data and method. Section 3 discusses the observational analysis. Section 4 discusses the modeling study. Section 5 summarizes the overall results with concluding remarks.

2. Data and method

The rainfall data used for this study are the Global Precipitation Climatology Project (GPCP) merged analysis of pentad precipitation (Xie et al. 2003) on a global 2.5° latitude × 2.5° longitude grid for the period 1979–2016. The pentad precipitation data are converted to daily data by first applying the pentad rainfall to each of the five days, and then using a 5-day running mean through the entire time series of each season. The EA rainfall is defined as the area mean of the rainfall over 110°–150°E, 20°–35°N (the black rectangle in Fig. 1).

The outgoing longwave radiation (OLR), which is closely related to rainfall in the tropics, is used to represent tropical convective activity. We use the new climate data record for daily OLR (Lee and NOAA CDR Program 2011; Schreck et al. 2018) from the High-Resolution Infrared Radiation Sounder (HIRS) sensors. The data are regridded to a global 2.5° × 2.5° resolution from its original 1° × 1° resolution. The daily wind variables used in this study are derived from National Centers for Environmental Prediction–Department of Energy (NCEP–DOE) atmospheric reanalysis (Kanamitsu et al. 2002). They are also on 2.5° × 2.5° grids.

The real-time multivariate MJO analysis developed by Wheeler and Hendon (2004, hereafter WH04) has been widely used in describing the MJO from real time observations. The analysis adopts an eight-phase structure to identify the evolution of the eastward-propagating MJO. The focus is usually on the active convection regime of each phase, which has been proven useful for forecasting tropical weather. The analysis is conducted by applying combined EOF analysis to 15°S–15°N latitudinally averaged OLR and zonal wind at 850 and 200 hPa (denoted as U850 and U200, respectively). The data are then high-pass filtered by subtracting out the previous 120-day running averaged anomalies from the seasonal cycle and interannual variability. The time series of the coefficients of daily fields of OLR, U850, and U200 projected onto the leading pair of the combined EOF modes (i.e., PC1 and PC2) are termed the RMM index. This approach enables the computation of the set of PCs as a real-time index to describe the MJO evolution. While the primary purpose of this index is to describe tropical convection, the approach differs from previous studies that used only OLR as the index, in that the RMM index is influenced more by the U850 and U200 components than OLR (Straub 2013; Kiladis et al. 2014).

TABLE 1. Summary of three MJO indices and corresponding data and methods.

MJO index	RMM (WH04)	RMM_DJFM	SVD
Leading mode	Combined EOF (OLR, U850, U200)		SVD (OLR, U850, U200)
Season	All season	DJFM	DJFM
Domain	Global tropics 15°S–15°N averaged		Global tropics U850, U200: 15°S–30°N OLR: 15°S–15°N

Because of the significant amplitude of the seasonal cycle in the tropical monsoon regions, the MJO exhibits considerable differences in spatial and temporal structure between boreal winter and summer (e.g., Kikuchi et al. 2012). Therefore, the RMM defined by all-season data may not be best suited for the studies of monsoon regional weather in a specific season. In this study of the East Asian winter rainfall, we will modify the RMM index by using boreal winter data (DJFM) only. The inclusion of March is desirable as the EA winter rainfall system reaches peak in February and March. Hereafter, we refer the wintertime RMM as RMM_DJFM index.

The singular value decomposition in this study uses the same three variables (OLR, U850, and U200) and filtering as in computing the RMM index, except the variables are two-dimensional fields. The OLR data cover the same global tropical belt (15°S–15°N) as in the RMM index. For the wind fields U850 and U200, the domain is expanded northward to cover the area of 15°S–30°N so that a substantial part of the East Asian winter rainfall region is included. The SVD analysis yields two leading groups of singular vectors consisting of spatial patterns of OLR, U850, and U200. The two leading singular vectors of U850 and U200 and the corresponding expansion coefficients are used to describe the spatial–temporal variation of the MJO. Hereafter, we refer the wind component of the wintertime MJO as SVD_DJFM index or simply SVD.

For a comparison, we summarize the three types of indices for the MJO and their variables in Table 1. Eight phases are used to describe one cycle for all three indices. The data used covers 37 years, 1979–2016.

3. Observational analysis

a. *The MJO indices and their spatial structures*

Many previous investigations used the EOF approach to show that the tropical convection associated with the MJO

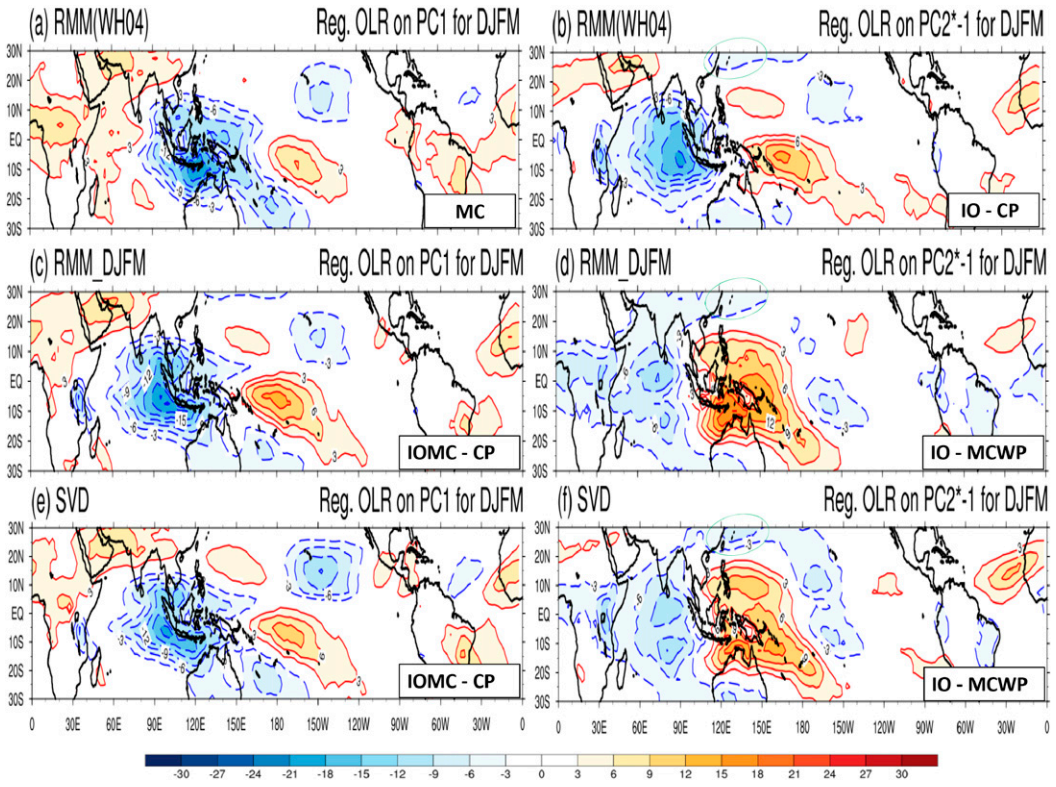

FIG. 2. Regressed OLR ($W\,m^{-2}$) fields against the reference time series of the two leading modes obtained by three approaches: (a),(b) RMM (WH04) for all seasons, (c),(d) RMM_DJFM, and (e),(f) SVD for winter seasons of December–March. RMM refers to the combined EOF analysis of daily OLR, U850, and U200 data averaged over the global tropical belt of 15°S–15°N. SVD refers to the SVD analysis of daily fields of OLR (15°S–15°N) and U850 and U200 (15°S–30°N). The second mode in (b), (d), and (f) is multiplied by −1. Only values with statistical significance (95% CI) are shaded. The green elliptic indicates the area of East Asian rainfall discussed in text.

evolution can be described effectively by two basic leading modes (e.g., Wheeler and Hendon 2004; Matthews 2008; Kikuchi et al. 2012; Kiladis et al. 2014; Hung and Sui 2018). Figure 2 shows the regression of daily OLR fields upon the two leading modes from three sets of indices: RMM (WH04) (Figs. 2a,b), RMM_DJFM (Figs. 2c,d), and SVD (Figs. 2e,f).

For the all-season RMM (WH04) regression, the first leading mode (Fig. 2a) is dominated by a center of activity over the Maritime Continent (MC) around 90°–150°E. The second leading mode (Fig. 2b) is characterized by a dipole with one center of activity over the Indian Ocean (IO) within 60°–120°E and another center of opposite phase over the central Pacific (CP) within 150°E–170°W. Hereafter, these two patterns are referred to as the MC mode and IO–CP mode, respectively. Around the region of the East Asian rainfall (green elliptic), the OLR anomaly in Fig. 2b is negative, indicating wet rainfall anomaly.

In the winter-only RMM_DJFM regression, the first mode (Fig. 2c) is similar to the IO–CP mode of the all-season RMM (WH04) regression (Fig. 2b), but with an eastward shift of around 20° longitude. Hereafter, we name this pattern the IOMC–CP mode. The second mode of RMM_DJFM (Fig. 2d) also has a somewhat dipole pattern, with the major center of activity over the Maritime Continent and subtropical western Pacific (MCWP) dominating over the weaker center of opposite sign over Indian Ocean. Hereafter, we name this asymmetric dipole pattern the IO–MCWP mode. It resembles somewhat the pattern of the second mode of the all-season RMM regression shown in Fig. 2b; it is also associated with wet East Asian rainfall anomaly (Fig. 2d).

The regressed OLR fields against the SVD index are shown in Figs. 2e and 2f. The first mode (Fig. 2e) is similar to the IOMC–CP dipole mode of the RMM_DJFM. The second mode (Fig. 2f) resembles the asymmetric IO–MCWP dipole mode from RMM_DJFM (Fig. 2d), but over the subtropical western North Pacific, the center of activity obtained from the SVD index has higher variances and more detailed structure, such that a secondary center appears east of the Philippines. This center is located south of the East Asian rainfall region where the negative OLR in Fig. 2f again indicates wet anomalies.

The first impression one can get from the above result is that EA rainfall anomalies are associated with the second leading mode (the IO–CP mode of RMM (WH04) and IO–MCWP mode of RMM_DJFM and SVD). When the all-season RMM (WH04) index is used, the most conspicuous feature is the IO-dominated mode (Fig. 2b). This is consistent with many previous studies that found that East Asian winter rainfall is related to the MJO when the MJO active convection is located

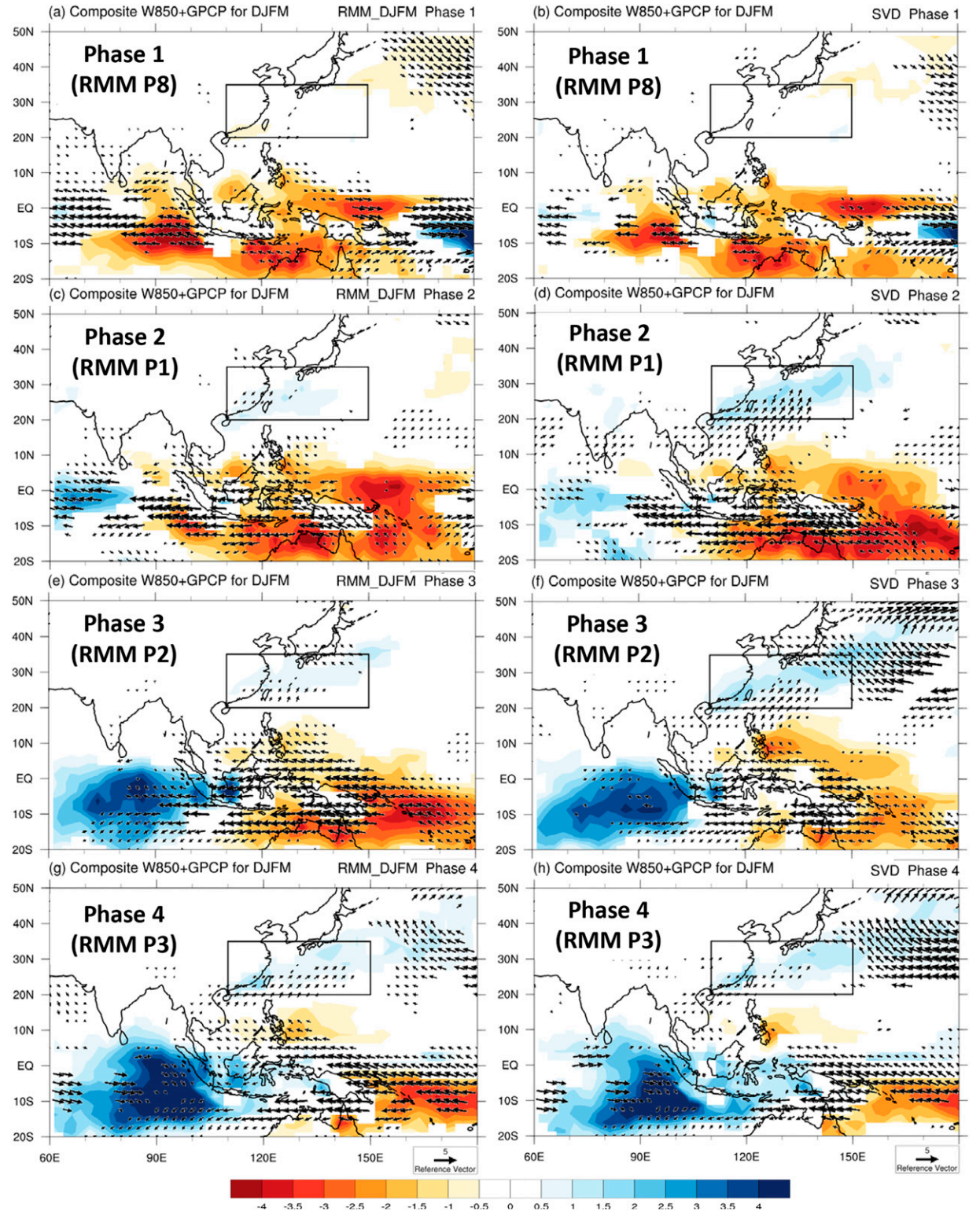

FIG. 3. Composite fields of anomalous GPCP rainfall (mm day^{-1}) and 850-hPa wind (m s^{-1}) for the half cycle of the MJO phases: (a),(c),(e),(g) phases 1, 2, 3, and 4 from RMM_DJFM and (b),(d),(f),(h) phases 1, 2, 3, and 4 from SVD. The half cycle of phase 1, 2, 3, and 4 corresponds to that of the all-season RMM phase P8, P1, P2, and P3 (in parentheses). Values only with statistical significance (95% CI) are shown.

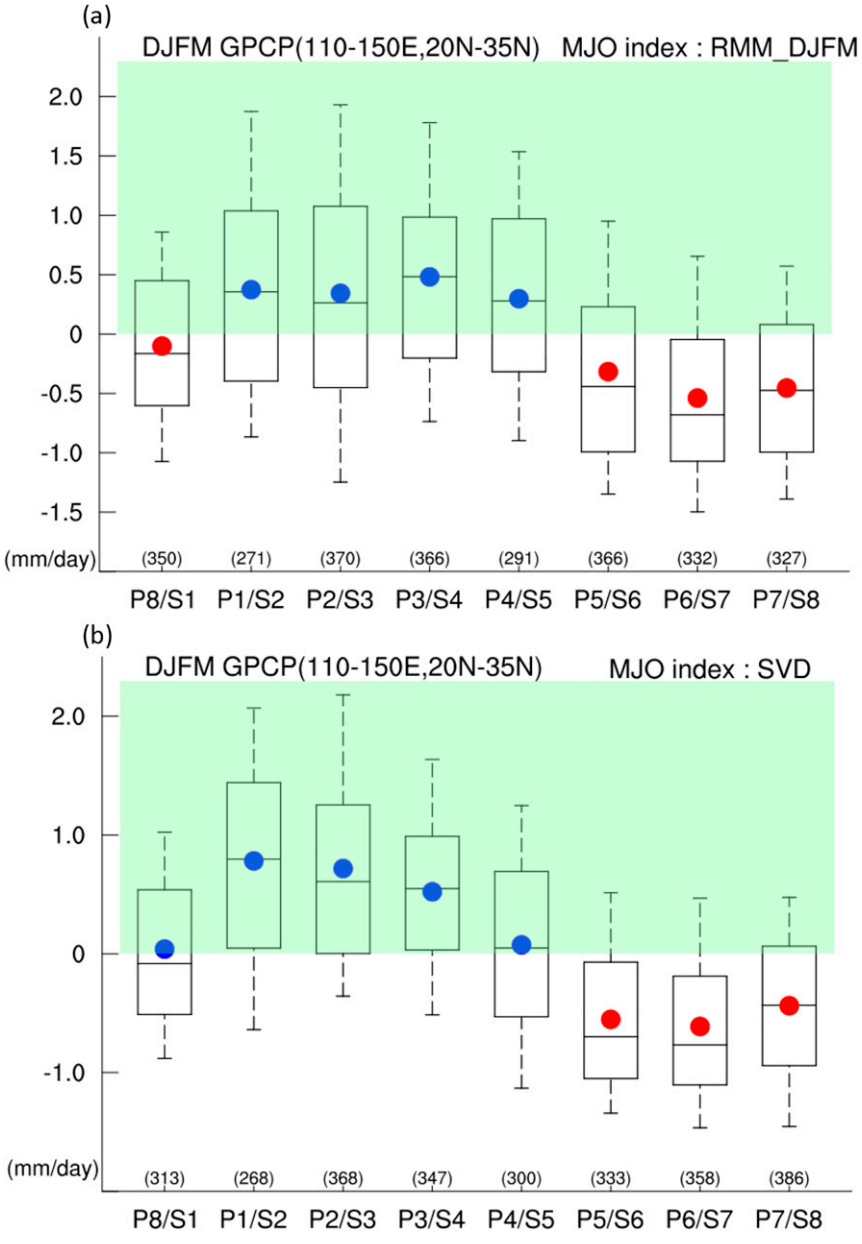

FIG. 4. Probability distribution of rainfall anomalies (mm day^{-1}) within the EA region (110°–150°E; 20°–35°N) in the eight phases of (a) RMM_ DJFM, and (b) SVD indices shown by box plots. Each box is drawn from the first quartile (bottom) to the third quartile (top), and a horizontal line is drawn through the box at the median with the mean value marked by solid dot; rainfall anomalies of 90% and 10% ranking are marked by the short horizontal line (–) linked to the box by dashed lines. Here the P and S numbers are the phases defined by all-season RMM and SVD, respectively. The number of days in each phase is shown in the parentheses above the horizontal axis.

in the Indian Ocean. However, when the RMM analysis is carried out using only boreal winter data, Fig. 2d suggests that a more important association appears to be the suppressed convection over the Maritime Continent and western Pacific. This location is much closer to the EA winter rainfall region than any MJO convection in the Indian Ocean. Apparently, the use of all-season data in RMM (WH04) blurred this aspect of the MJO–EA winter rainfall relationship. When the two-dimensional SVD index is used, the pattern suggesting this relationship becomes even more conspicuous with the secondary center east of the Philippines located adjacent to the East Asian winter rainfall region. This MJO–EA winter rainfall relationship shown in the winter data analysis indicates the importance of convective activities over MC and subtropical western North

Pacific, which is different from the relationship associated with the IO dominated mode.

b. *The MJO phase composites and East Asian rainfall probability distribution*

The composite fields of anomalous rainfall (GPCP) and 850-hPa wind with respect to the RMM_DJFM index are shown in the left columns of Fig. 3 (Figs. 3a,c,e,g), and those with respect to the SVD index are shown in the right column of Figs. 3b,d,f,h. For both indices only one-half cycle (phases 1, 2, 3, and 4) is shown.

The use of only the boreal winter data in the RMM_DJFM and SVD indices causes a shift of near one-eighth of a cycle from the all-season RMM (WH04), such that the four phases in Fig. 3 may be comparable to phases P8, P1, P2, and P3 of the RMM (WH04), respectively. Because of the widely used convention and familiarity of the original RMM (WH04) phases, there may be a confusion when we mention a particular phase of the RMM_DJMF and the SVD indices. Therefore, we will adopt a name system that is consistent with the commonly used definition of RMM phases. In the following discussions whenever a phase is identified by a P number, it is equivalent to the phase number of RMM (WH04). So P1, P2, P3, P4, P5, P6, P7, and P8 are used to refer to RMM_DJMF phases 2, 3, 4, 5, 6, 7, 8, and 1, respectively.

The two sets of wind and rainfall (GPCP) fields in Fig. 3 show a common overall evolution. Suppressed convection propagates eastward from East Indian Ocean and Maritime Continent in phase 1 (RMM P8) to the central Pacific near the date line in phase 4 (RMM P3). To its west the initiation of active convection occurs over western Indian Ocean, enhances, and propagates eastward to the eastern Indian Ocean and western Maritime Continent in phase 4 (RMM P3). Accompanying the evolution of the convection activity, positive rainfall anomalies over the EA region (110°–150°E, 20°–35°N, indicated by the rectangular box in Fig. 3) appear in phases 2, 3, and 4 (RMM P1–P3) for both indices. However, the EA rainfall anomalies are considerably stronger in the SVD composite (Figs. 3d,f,h) than in the RMM_DJFM composite (Figs. 3c,e,g). In the SVD composite the southerly component wind anomalies south of the slowly eastward moving EA rainfall belt, particularly in phases 2 and 3 (RMM P1–P2), are stronger than in the RMM_DJFM composite. This indicates a relationship such that the MJO enhances the EA rainfall through low-level wind convergence in phases 2, 3, and 4 (RMM P1–P3) and is consistent with the appearance of suppressed convection south of the EA rainfall wet anomalies shown in Fig. 2. This relationship is revealed clearly in the SVD index composite but is more ambiguous when the RMM_DJFM index is used.

The advantage of SVD in isolating the effect of the MJO on East Asian winter rainfall can also be seen in the events probability distribution of EA rainfall anomalies over the eight phases. Figures 4a and 4b show the box plots for the eight phases based on the RMM_DJFM and SVD indices, respectively. Here the phase based on RMM (WH04) (P1, P2, . . . , P8) and the phase based on RMM_DJFM and SVD (S1, S2, . . . , S8) are both shown in the figure. In the distribution based on

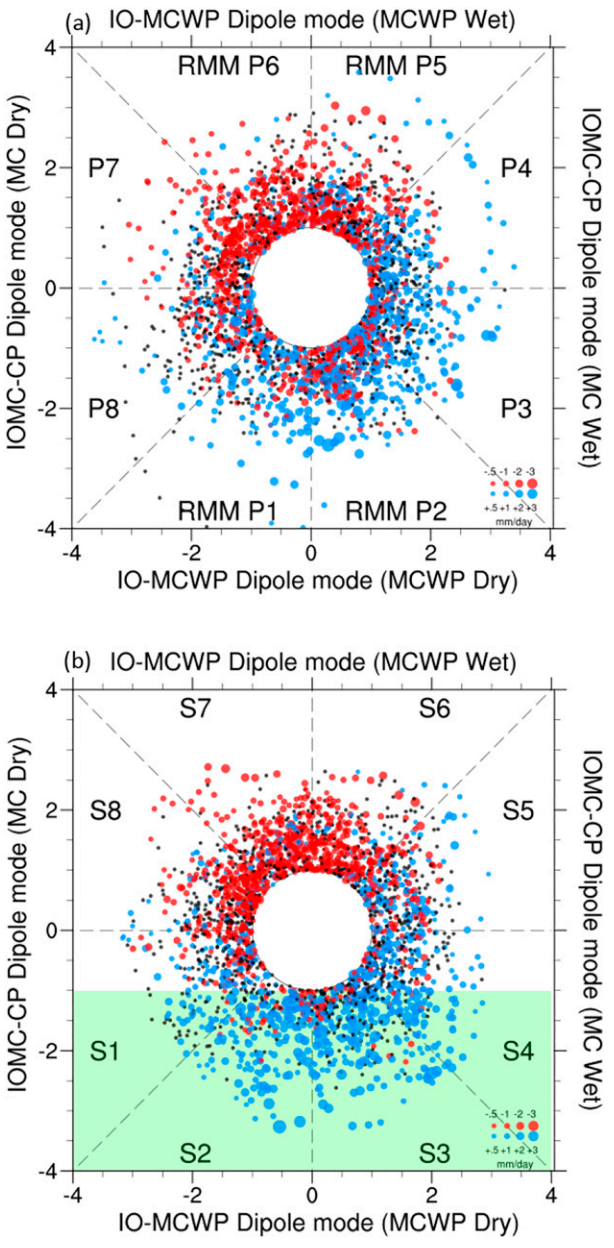

FIG. 5. Rainfall anomalies in the EA region (110°–150°E, 20°–35°N) displayed in the (PC1, PC2) phase space based on (a) RMM_DJFM and (b) SVD indices. The eight phases labeled in (a) are based on all-season RMM (P1, P2, . . . , P8) and in (b) based on SVD (S1, S2, . . . , S8). The magnitude of rainfall anomalies is shown by the size of the dots and the sign by color (red for below normal −3, −2, −1, −0.5; black for normal from −0.5 to 0.5; blue for above normal 0.5, 1, 2, 3 mm day^{-1}). The phase domain for SVD-based PC2 $< -1\sigma$ in (b) is shaded in green.

RMM_DJFM index (Fig. 4a), the mean rainfall anomalies (the blue/red dot points), which are close to the medium values, are positive in phases 2, 3, 4, and 5 (RMM P1–P4) with values of 0.4, 0.3, 0.5, and 0.3 mm day^{-1} respectively, whereas they are negative in phases 6, 7, 8, and 1 (RMM P5-P8), with values

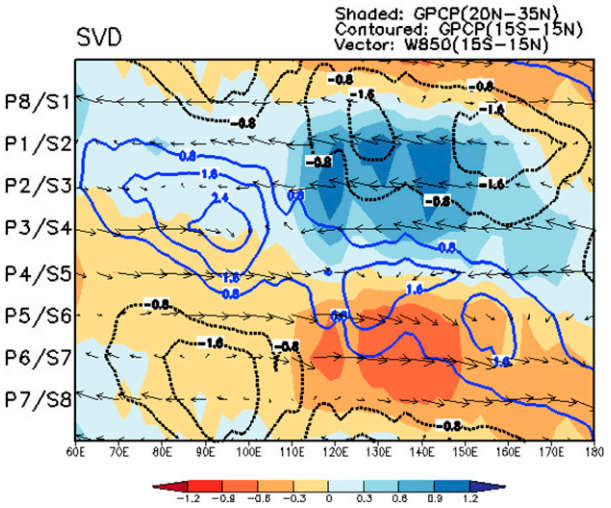

FIG. 6. Phase–longitude diagram of composite 850-hPa wind and rainfall anomalies latitudinally averaged in the tropical belt 15°S–15°N (contours) and subtropical belt 20°–35°N (shaded). Positive and negative contours are colored in blue and black, respectively; the contour interval is 0.8 mm day^{-1}.

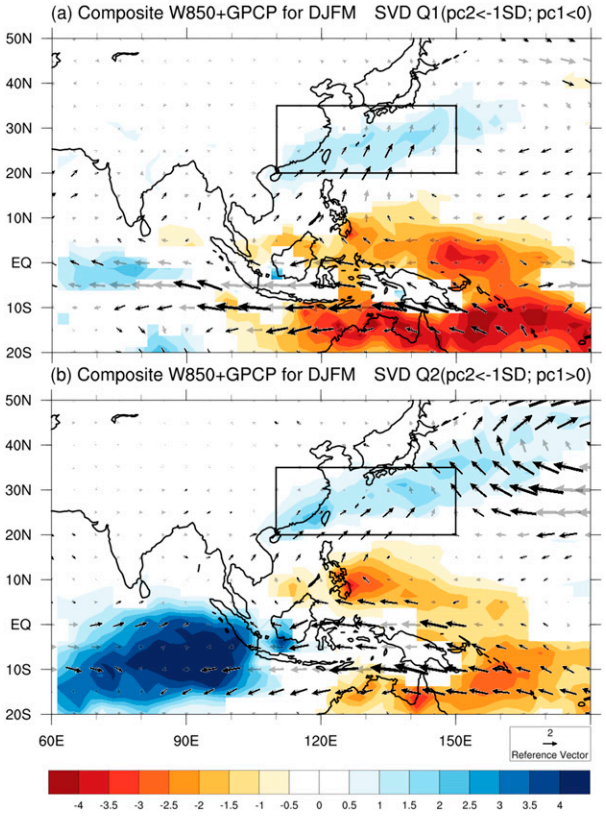

FIG. 7. Composite fields of anomalous GPCP rainfall (mm day^{-1}) and 850-hPa wind (m s^{-1}) for the days when PC2 of the SVD analysis $< -1\sigma$ and (a) PC1 < 0, (b) PC1 > 0, within the green shaded domain in the phase plane in Fig. 5b. The number of days in composite (a) is 309 and (b) is 433. Rainfall anomalies with statistical significance (95% CI) are shaded. Wind anomalies with statistical significance are shown in dark wind vector, and the rest are shown in gray.

of −0.3, −0.5, −0.5, and −0.1 mm day^{-1}, respectively. This result is consistent with the findings in previous studies using the RMM (WH04) index (e.g., Hung et al. 2014; Jeong et al. 2008; Jia et al. 2011), in which the EA wet period is more related to the first half cycle of the MJO (centered at RMM P2–P3) and the EA dry period is more related to the second half cycle of the MJO (centered at RMM P6–P7).

In the distribution based on the SVD index (Fig. 4b) the separation between the positive and negative anomalies is sharper (i.e., the probability of both wet and dry events is concentrated in only three phases). The rainfall anomalies in the wet phases (S2–S4, or RMM P1–P3) have mean values of 0.8, 0.7, and 0.5 mm day^{-1}, respectively, which are more concentrated than those of the RMM_DJFM results spreading over four phases and without a consistent trend from one phase to the next. The mean rainfall anomalies in the dry phases (S6–S8, or RMM P5–P7) have values of −0.6, −0.6, and −0.4 mm day^{-1}, respectively, which are also more concentrated than those of the RMM_DJFM results. This better identification of the MJO influences is also reflected in the rainfall probability distribution itself. Figure 4 shows the rainfall probability in EA during the eight MJO phases. During the four wet phases of the RMM_DJFM (Fig. 4a), the probability for positive rainfall anomalies is higher than 60%–70% (and less than 30%–40% for negative rainfall anomalies), whereas during the three SVD wet phases the probability of positive rainfall anomalies is higher than 75% (and less than 25%, the lower boundary of the boxes, for negative rainfall anomalies). The same type of contrast can also be seen in the rainfall probability distribution of the dry phase's cases.

The previous figures are regression or composite diagrams. Figures 5a and 5b present the scatterplots of all individual rainfall cases in a phase space for the RMM_DJFM and SVD analyses, respectively. Here the horizontal coordinate is PC1, and the vertical coordinate is PC2. The two coordinates can be described by the IOMC–CP dipole and IO–MCWP dipole modes, respectively. The clustering of negative (red) and positive (blue) EA rainfall anomalies in the upper and lower half of the phase diagram can be seen in both figures, but the separation between the two anomaly regimes is obviously clearer in the SVD diagram (Fig. 5b) than in the RMM_DJFM diagram (Fig. 5a). This distribution indicates again that the second mode of RMM_DJFM and SVD, or the IO–MCWP mode, is the important mode that represent the EA rainfall anomalies, and that EA wet period begins in the middle of SVD phase 1 (RMM P8) when the number of dry cases diminishes. This is indicated in the green-shaded domain of Fig. 5b in which most cases are wet anomaly cases.

c. *Indian Ocean forcing versus Maritime Continent–western Pacific forcing*

To further examine the time evolution of the MJO–EA winter rainfall relationship, we show the phase–longitude distribution of three latitudinally averaged variables: tropical rainfall and wind at 850 hPa (15°S–15°N) and extratropical rainfall (20°–35°N) in Fig. 6. The evolution is described in four stages during

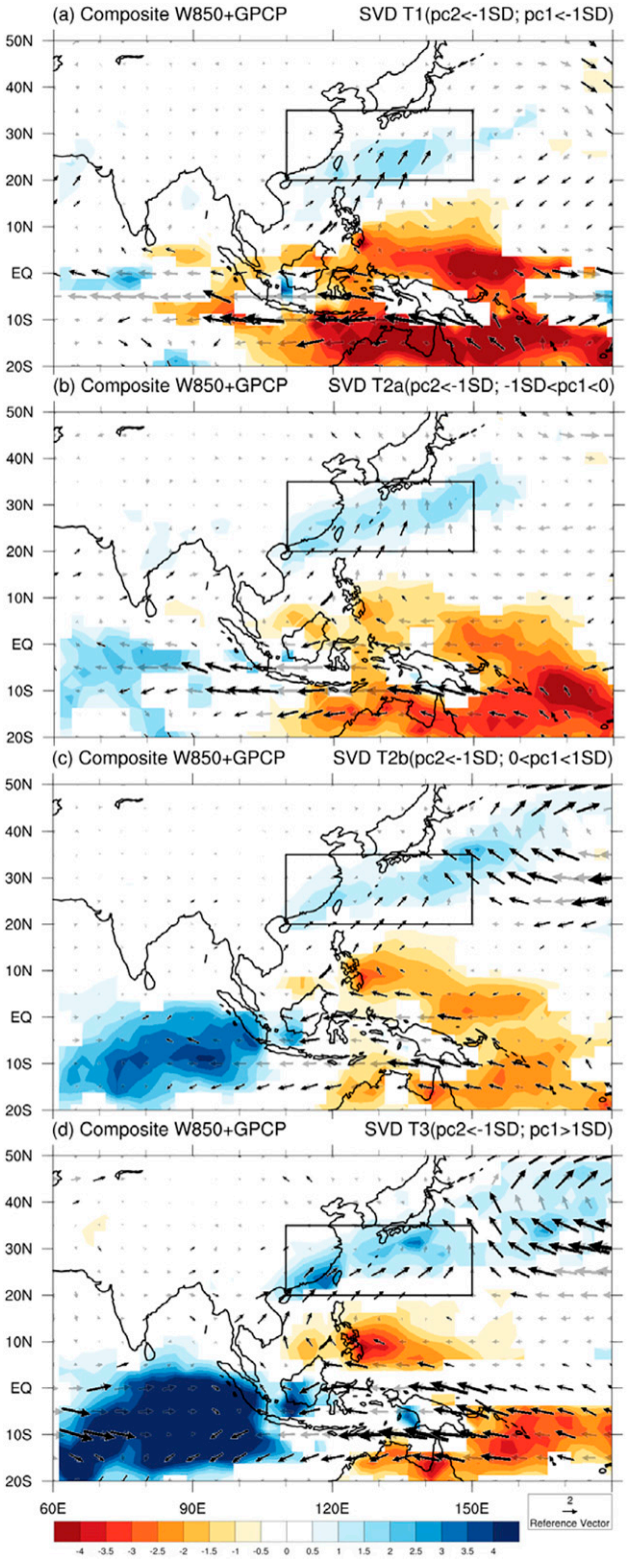

FIG. 8. Composite fields of anomalous GPCP rainfall (mm day^{-1}) and 850-hPa wind (m s^{-1}) for the days when PC2 of the SVD analysis $< -1\sigma$ and (a) PC1 $< -1\sigma$, (b) $-1\sigma <$ PC1 < 0, (c) $0 <$ PC1 $< 1\sigma$, and (d) PC1 $> 1\sigma$, within the green shaded domain in the phase plane in Fig. 5b. The number of days in (a), (b), (c), and (d) is 124, 185, 272, and 161, respectively. Rainfall anomalies with statistical significance (95% CI) are shaded. Wind anomalies with statistical significance are shown in dark wind vectors; the rest are shown in gray.

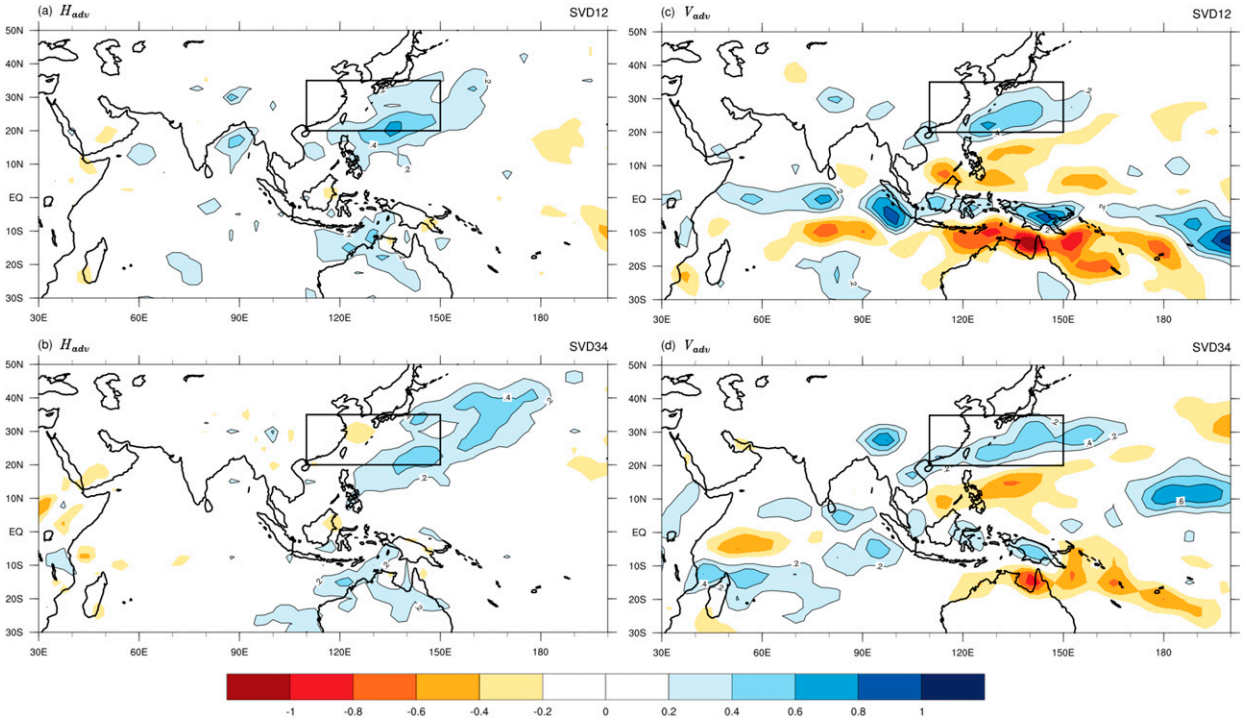

FIG. 9. The horizontal fields of vertically integrated moisture budget: (a),(b) horizontal advection for SVD12 and SVD34 and (c),(d) vertical advection for SVD12 and SVD34 (units are g kg^{-1} day^{-1}). The positive values are shaded and also contoured.

the eastward propagation of MJO. In stage 1 (SVD phases 1–2, or RMM P8–P1), suppressed tropical rainfall (dotted contours) over MCWP leads the EA positive rainfall anomaly (blue color) by about one phase; the latter becomes most enhanced in SVD phase 2–3 (RMM P1–P2). The easterly anomalies over IO associated with the suppressed convection over MC in stage 1 transport moisture for the initiation and development of the MJO over the IO (Zhao et al. 2013; Kim et al.2014; Tseng et al. 2015; Hung and Sui 2018) in the following stage 2 (SVD phase 3–4, or RMM P2–P3). The positive tropical rainfall anomalies over IO (blue contours) and negative values over MCWP (dotted contours), the IO–MCWP dipole, coincides with enhanced rainfall in EA. In stage 3 (SVD phase 5–6, or RMM P4–P5), enhanced tropical rainfall in MCWP leads suppressed rainfall in EA by about one phase, which persists through stage 4 (SVD phase 7–8, RMM P6–P7). The tropical rainfall dipole in stage 4 is opposite to that of stage 2.

The spatial distribution of the tropical–extratropical rainfall and circulation in stages 2 (RMM phase P2–P3) has been discussed in previous studies. The EA rainfall anomaly is generally explained in these previous studies as the Rossby wave flow forced by the MJO heating over IO in stage 2, interacting with mean flow in the EA jet entrance region (e.g., Kim et al. 2006; Jeong et al. 2008; He et al. 2011). On the other hand, our SVD analysis in Figs. 4b, 5b, and 6 shows that enhanced EA rainfall starts earlier from the middle of SVD phase 1 (RMM P8). The most frequent rainfall events in EA occur during SVD phases 2 and 3 (RMM P1–P2), when convection develops over IO while MCWP remains suppressed (Figs. 2 and 3).

This earlier relationship can be examined by composites of precipitation and 850-hPa wind for the days corresponding to PC2 $< -1\sigma$ in SVD phase 1–4 (green shaded domain in Fig. 5b) in two groups: PC1 < 0 and PC1 > 0. The days in group 1 (309) consists of a small subset of SVD phases 1 (41 days) and a full set of phase 2 (268 days), and the days in group 2 (433) consist of a full set of SVD phases 3 (368 days) and a small subset of phases 4 (65 days). The composite fields of anomalous rainfall and 850-hPa wind for the two groups are shown in Fig. 7. The figure shows two contrasting dipoles of tropical rainfall of negative anomalies over MCWP and positive anomalies over east IO with the former much stronger in group 1 (Fig. 7a) and the latter stronger in group 2 (Fig. 7b).

Associated with the tropical heating, the composite fields for group 1 (Fig. 7a) show a close link of the suppressed rainfall over tropical MC and western Pacific (20°S–15°N, 110°–180°E), anticyclonic flow at 850 hPa and enhanced rainfall in EA (20°–35°N, 110°–150°E, denoted in Fig. 7 by the black rectangular box). Figure 7a suggests that suppressed convection over MCWP weakens the meridional overturning circulation in East Asian winter monsoon between the MCWP divergent flow and the EA jet (e.g., Chang and Lau 1982; Chang et al. 2005). The anomalous southwesterly component of the MCWP divergent flow supplies moisture to EA rainfall system as shown in the moisture budget analysis shown in the next subsection.

The composite fields for group 2 (Fig. 7b) show that the zonally asymmetric rainfall dipole (strong positive anomaly over east IO and weak negative anomaly over MCWP) is

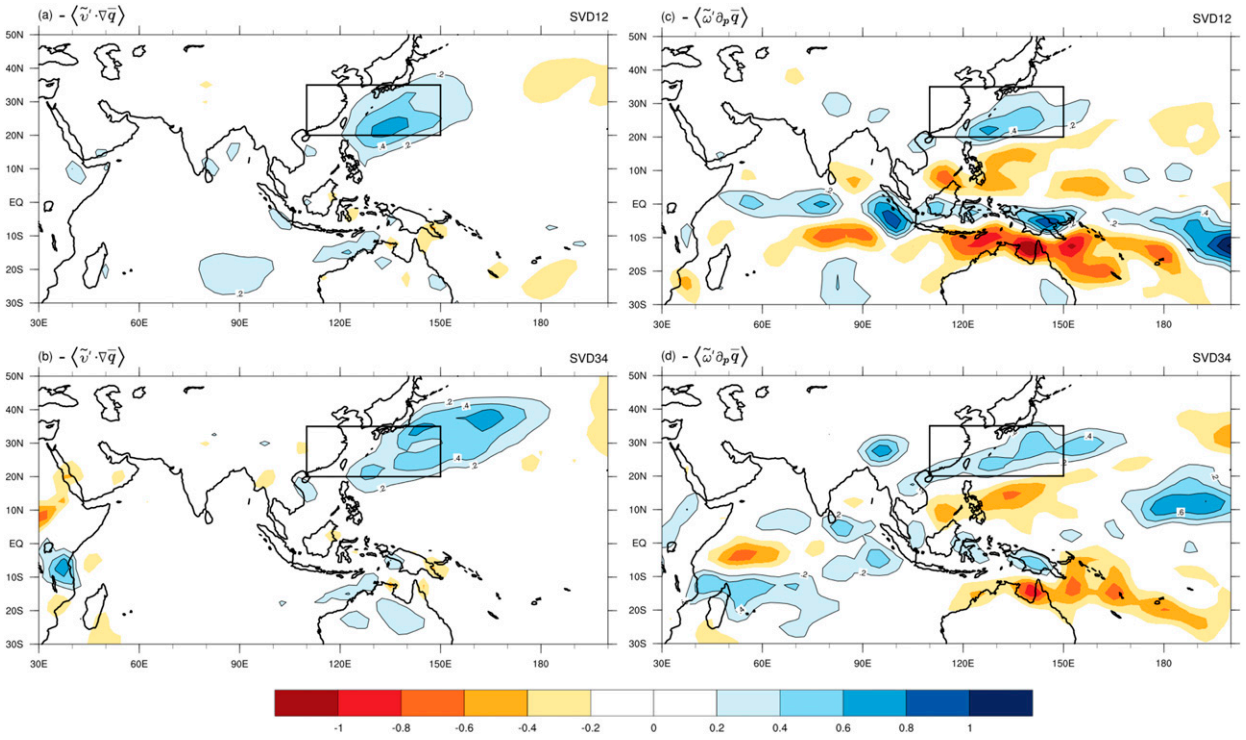

FIG. 10. As in Fig. 9, but for the dominant component: $-\langle\tilde{\mathbf{v}}'\partial_p\bar{q}\rangle$ and $-\langle\tilde{\omega}'\partial_p\bar{q}\rangle$ (g kg^{-1} day^{-1}). The positive values are shaded and also contoured.

associated with cyclonic circulation over IO and anticyclonic circulation over MCWP. The anomalous southwesterly component of the MCWP divergent flow here is part of the forced Rossby wave gyre in response to the MJO dipole heating.

Although the anomalous southwesterly wind in group 1 (Fig. 7a) and group 2 (Fig. 7b) are all associated with MCWP divergent flow, our result suggests two mechanisms for the MJO–EA rainfall relation. The dominant forcing for the EA rainfall in group 1 is the suppressed convection in MCWP and that in group 2 is convective heating in IO. Note that the extratropical anticyclonic circulation east of the EA box in both groups is part of the quasigeostrophic responses along with the EA ascending motion resulted primarily from the MCWP cooling as supported by the modeling experiments in section 4.

We further classify days corresponding to PC2 $< -1\sigma$ in SVD phase 1–4 (green shaded domain in Fig. 5b) into four groups for the four intervals of PC1: less than -1σ, from -1σ to 0, from 0 to 1σ, and greater than 1σ. The composite fields of rainfall and 850-hPa wind are shown in Fig. 8. The figure shows a systematic evolution of MJO convection with the suppressed MCWP rainfall gradually diminishes and IO rainfall gradually increases through the four temporal groups. The overall evolution of tropical convection anomalies signals the development of the IO–MCWP dipole and the distinct low-level anticyclonic flow south of the EA rainfall band. Note that the anticyclonic flow and the suppressed convection over MCWP develops (in S1/S2) ahead of the IO rainfall (in S3/S4), suggesting the suppressed MCWP convection as the cause of weakened winter monsoon, EA ascending motion, and the associated meridional moisture advection in the lower troposphere that all contribute to the EA rainfall before the IO–MCWP heating-induced Rossby wave teleconnection becomes dominant.

d. Moisture budgets

The role of moisture supplies to the MJO has been emphasized by previous studies (e.g., Hsu and Li 2012; Tseng et al. 2015, and references therein). To show the contribution to the EA rainfall by moisture transport in the SVD phase 1–2 versus phase 3–4, we calculate the vertically integrated moisture budget in the lower troposphere based on the following scale separation of the moisture budget equation:

$$\partial_t q = -\mathbf{v}\cdot\nabla q - \omega\partial_p q - L^{-1}Q_2. \tag{1}$$

The budget equation can be written in terms of basic and anomalous components (i.e., $q=\overline{q}+q'$, $\mathbf{v}=\overline{\mathbf{v}}+\mathbf{v}'$, $\omega=\overline{\omega}+\omega'$), and the difference of Eq. (1) and the time mean of (1) gives

$$\begin{aligned}\partial_t q' = &-\mathbf{v}'\cdot\nabla\overline{q} - \overline{\mathbf{v}}\cdot\nabla q' - \mathbf{v}'\cdot\nabla q' + \overline{\mathbf{v}'\cdot\nabla q'} - \omega'\partial_p\overline{q}\\ &- \overline{\omega}\partial_p q' - \omega'\partial_p q' + \overline{\omega'\partial_p q'} - L^{-1}(Q_2 - \overline{Q_2}).\end{aligned} \tag{2}$$

Then the phase composite of (2) can be written as

$$\begin{aligned}\partial_t \tilde{q}' = &-\tilde{\mathbf{v}}'\cdot\nabla\overline{q} - \overline{\mathbf{v}}\cdot\nabla\tilde{q}' - \widetilde{\mathbf{v}'\cdot\nabla q'} + \overline{\mathbf{v}'\cdot\nabla q'} - \tilde{\omega}'\partial_p\overline{q}\\ &- \overline{\omega}\partial_p\tilde{q}' - \widetilde{\omega'\partial_p q'} + \overline{\omega'\partial_p q'} - L^{-1}(\widetilde{Q_2} - \overline{Q_2}).\end{aligned} \tag{3}$$

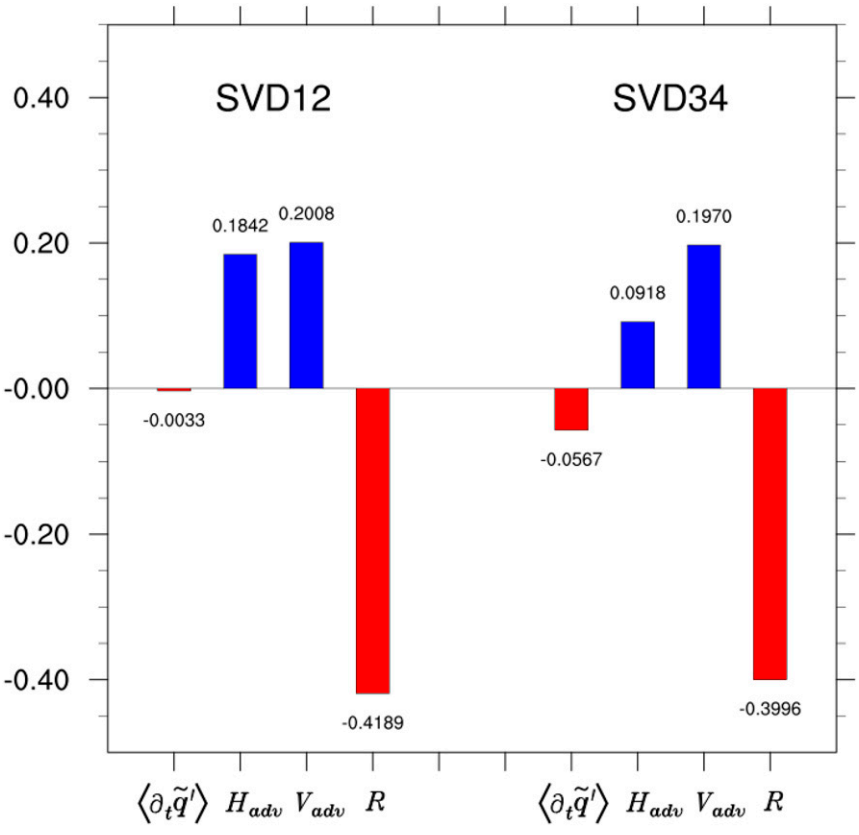

FIG. 11. The areal mean of vertically integrated moisture budget within the EA region (110°–150°E, 20°–35°N) for SVD phase 1–2 and SVD phase 3–4. The budget terms shown include the tendency, Hadv, Vadv, and $R = -L^{-1}(\langle \widetilde{Q_2} \rangle - \overline{Q_2})$ (units are g kg^{-1} day^{-1}).

We calculate the vertically integrated anomalous budgets (3)

$$\text{Hadv} = -\langle \tilde{\mathbf{v}}' \cdot \nabla \overline{q} \rangle - \langle \overline{\mathbf{v}} \cdot \nabla \tilde{q}' \rangle - \langle \widetilde{\mathbf{v}' \cdot \nabla q'} \rangle + \langle \overline{\mathbf{v}' \cdot \nabla q'} \rangle, \quad (4)$$

$$\text{Vadv} = -\langle \tilde{\omega}' \partial_p \overline{q} \rangle - \langle \overline{\omega} \partial_p \tilde{q}' \rangle - \langle \widetilde{\omega' \partial_p q'} \rangle + \langle \overline{\omega' \partial_p q'} \rangle, \quad (5)$$

$$R = -L^{-1}(\langle \widetilde{Q_2} \rangle - \overline{Q_2}), \quad (6)$$

where the angle brackets denote vertical integration through four layers centered at 1000, 925, 850, and 700 hPa.

The composite budgets for the days corresponding to PC2 $< -1\sigma$ in SVD phase 1–4 (green shaded domain in Fig. 5b) in the two groups PC1 < 0 and PC1 > 0 are shown in Fig. 9. In the group of SVD phase 1–2 (or simply SVD12), both horizontal and vertical moisture advection (Hadv in Fig. 9a and Vadv in Fig. 9c) show moistening in the EA region (marked by the rectangle) where enhanced rainfall consumes the moisture source. The advective moistening (Fig. 9a) supports the process by anomalous southwesterly component of the MCWP divergent flow to transport the moist air from tropical warm pool to EA region (Fig. 7a). The moisture budget for the group of SVD phase 3–4 (or simply SVD34) in Figs. 9b and 9d show similar features to that for SVD12, indicating the same advective processes are working. We further examine each component of the Hadv and Vadv in the scale separated budgets in (4) and (5). The results show that $-\langle \tilde{\mathbf{v}}' \cdot \nabla \overline{q} \rangle$ and $-\langle \tilde{\omega}' \partial_p \overline{q} \rangle$ are the dominant budget terms as shown in Fig. 10 for both SVD12 and SVD34. The overall distribution and magnitude of the budgets in Fig. 10 resemble those in Fig. 9, indicating that Hadv and Vadv are contributed primarily by advection of mean moisture field by intraseasonal flow $-\langle \tilde{\mathbf{v}}' \cdot \nabla \overline{q} \rangle$ and $-\langle \tilde{\omega}' \partial_p \overline{q} \rangle$, respectively, for both SVD12 and SVD34.

A more quantitative comparison of the budgets in the EA region (110°–150°E, 20°–35°N) is shown in Fig. 11. The budgets in Figs. 10 and 11 show a near balance between the anomalous advective moistening (of both the horizontal and vertical components) and condensation drying in both groups, and that total advective moistening in SVD12 (0.38 g kg^{-1}day^{-1}) is larger than that in SVD34 (0.29 g kg^{-1}day^{-1}). The budget further shows that the horizontal advection in SVD 12 (0.18 g kg^{-1}day^{-1}) is larger than that in SVD 34 (0.09 g kg^{-1}day^{-1}), indicating a more significant role of the horizontal moisture advection in SVD12 than that in SVD34.

4. Forced experiments by a linear baroclinic model

Previous studies have shown that the MJO-induced teleconnection is dominated by linear dynamics (Mori

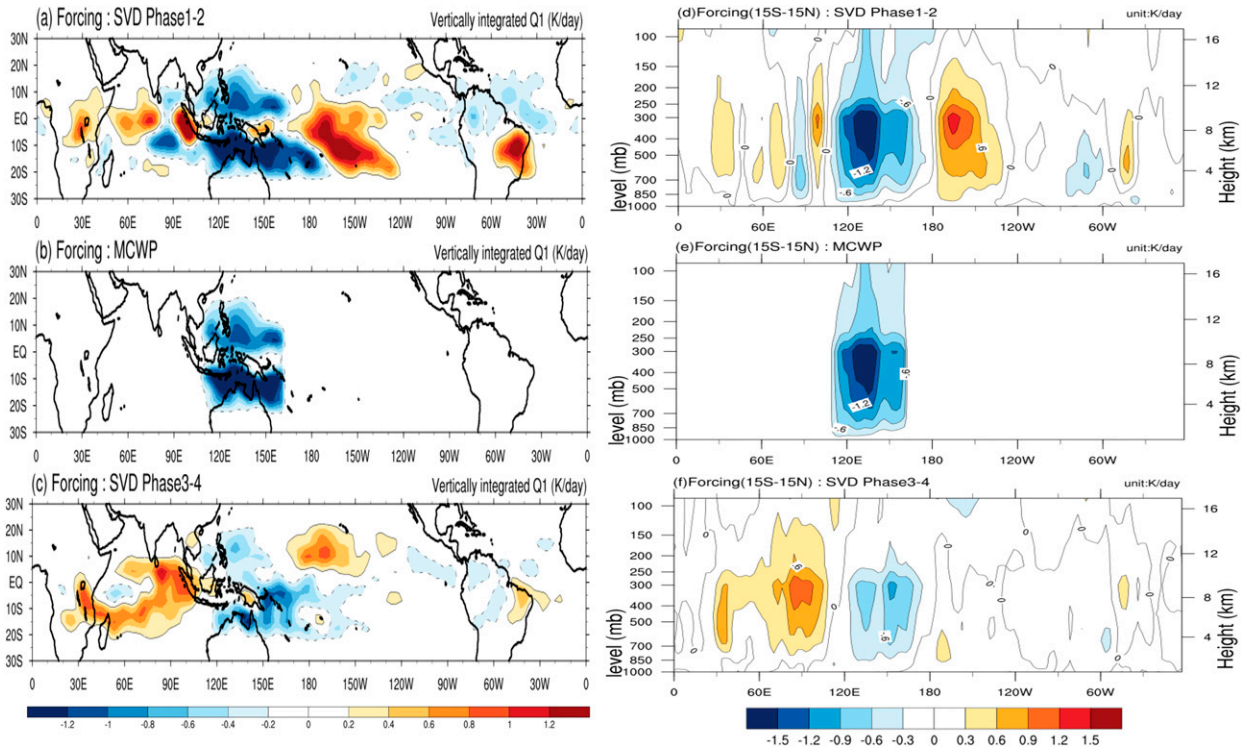

FIG. 12. (a)–(c) The horizontal distribution of vertically integrated Q_1' and (d)–(f) the vertical–zonal distribution of latitudinally averaged Q_1' within 15°S–15°N for SVD12, MCWP, and SVD34, respectively. Units are K day^{-1}. Thin solid and dashed lines enclosing the heating and cooling fields in (a)–(c) are 0.2 and −0.2 K day^{-1} contours.

and Watanabe 2008; Tseng et al. 2019). In this section, we use the linear baroclinic model (LBM) by Watanabe and Kimoto (2000) to examine the mechanisms of tropical–extratropical teleconnections discussed in section 3c. The model is constructed on primitive equations linearized about prescribed basic states. The vertical and horizontal resolutions of the model are 20 sigma levels and T42, respectively. Rayleigh friction and Newtonian cooling are employed in the model with an *e*-folding time of 20 days in most model layers except the top two layers and the bottom three layers where the *e*-folding time is 0.5 days. A fourth-order biharmonic damping (∇^4) with an *e*-folding time of 2 h is applied to damp the shortest wavenumber.

We perform experiments to simulate the phase-dependent teleconnection responses similar to the approach in Tseng et al. (2019). The model basic states are derived from the European Centre for Medium-Range Weather Forecasts (ECMWF) third-generation reanalysis product (ERA-Interim; Dee et al. 2011) by temporally averaging fields of variable during the extended boreal winter (November to March) from 1979 to 2015. The daily mean apparent heat source Q_1 defined by Yanai et al. (1973)

$$Q_1 = \partial_t s + \mathbf{v}\cdot\nabla s + \omega\partial_p s \tag{7}$$

defined by dry static energy ($s = c_pT + gz$) is used to representing the MJO forcing. The term Q_1 represents a collective effect of radiative cooling and subgrid-scale processes including condensation heating, evaporation, and eddy heat flux convergence. The anomalous Q_1 is derived by removing the first three harmonics of the seasonal cycle.

We conduct three experiments to test the teleconnection response to the variations of the MJO forcing. The first two experiments use the composite $Q_1' = \widetilde{Q_1} - \overline{Q_1}$ corresponding to SVD phase 1–2 and SVD phase 3–4, respectively. To further examine the forced response to negative heating in MCWP, we perform another experiment by imposing the same composite Q_1' as in SVD12 except within the area 110°–160°E with negative heating only (hereafter referred to as MCWP). To ensure only tropical forcing is considered, only Q_1' within 20°S–20°N is imposed in all three experiments.

TABLE 2. Summary of the derivation of the MJO heating (Q_1') and the spatial distribution of Q_1' imposed in the three experiments.

Expt ID	Composite Q_1' in time (imposed area)	Spatial distribution of Q_1'
SVD12	MJO SVD phase 1–2, PC2 $< -1\sigma$ (20°S–20°N)	Figs. 12a,d
SVD34	MJO SVD phase 3–4, PC2 $< -1\sigma$ (20°S–20°N)	Figs. 12c,f
MCWP	MJO SVD phase 1–2, PC2 $< -1\sigma$ (20°S–20°N, 110°–160°E, negative heating only)	Figs 12b,e

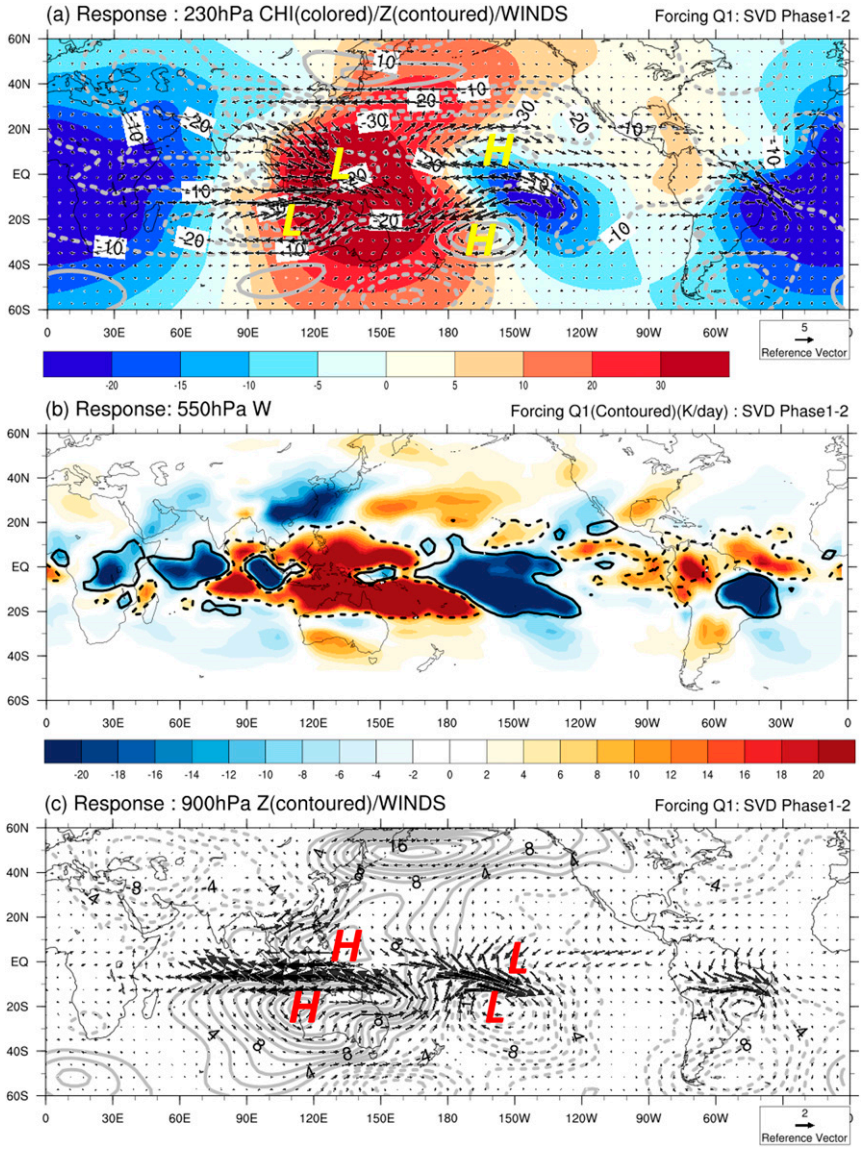

FIG. 13. Model simulated fields in SVD12 (a) horizontal wind (vectors), height (contour; interval 10 m), and velocity potential (shading) at 230 hPa, (b) vertical velocity at 550 hPa (shading) along with $Q_1' = 0.2$ and -0.2 K day^{-1} contours (as in Fig. 8a), and (c) horizontal wind (vectors), height (contour; interval 2 m) at 900 hPa.

The spatial distribution of Q_1' imposed in the three experiments is shown in Fig. 12 by the horizontal fields of vertically integrated Q_1' (Figs. 12a,b,c) and the vertical–zonal distribution of latitudinally averaged Q_1' within the tropical belt (15°S–15°N) (Figs. 12d,e,f). The vertically integrated Q_1' for SVD12 (Fig. 12a) and SVD34 (Fig. 12c) resembles the composite GPCP rainfall anomalies in Figs. 7a and 7b as expected because of the same days for the MJO composite. The vertical distribution of Q_1' for SVD12 and SVD34 (Figs. 12d,f) is characterized by deep anomalous heating profiles with peak values centered around the 300–400-hPa layer where maximum cooling and heating reach -1.5 and 1 K day^{-1}, respectively. The derivation of the heating (Q_1') and the spatial distribution of Q_1' for the three experiments are summarized in Table 2.

The LBM responses to the imposed tropical heating in the three experiments show a general pattern of a fast growth rate in the first pentad, a slower growth in the second pentad, and a quasi-steady state in the third pentad. For brevity, we choose to only show model responses at day 15 when the simulated fields are representative of the responses in the third pentad. The simulated horizontal winds and height fields at 900 and 230 hPa and vertical p velocity at 550 hPa for the three experiments SVD12, MCWP, and SVD34 are shown in Figs. 13, 14, and 15, respectively. The overall responses in the three experiments consist of the forced tropical wave signals within 20°S and 20°N

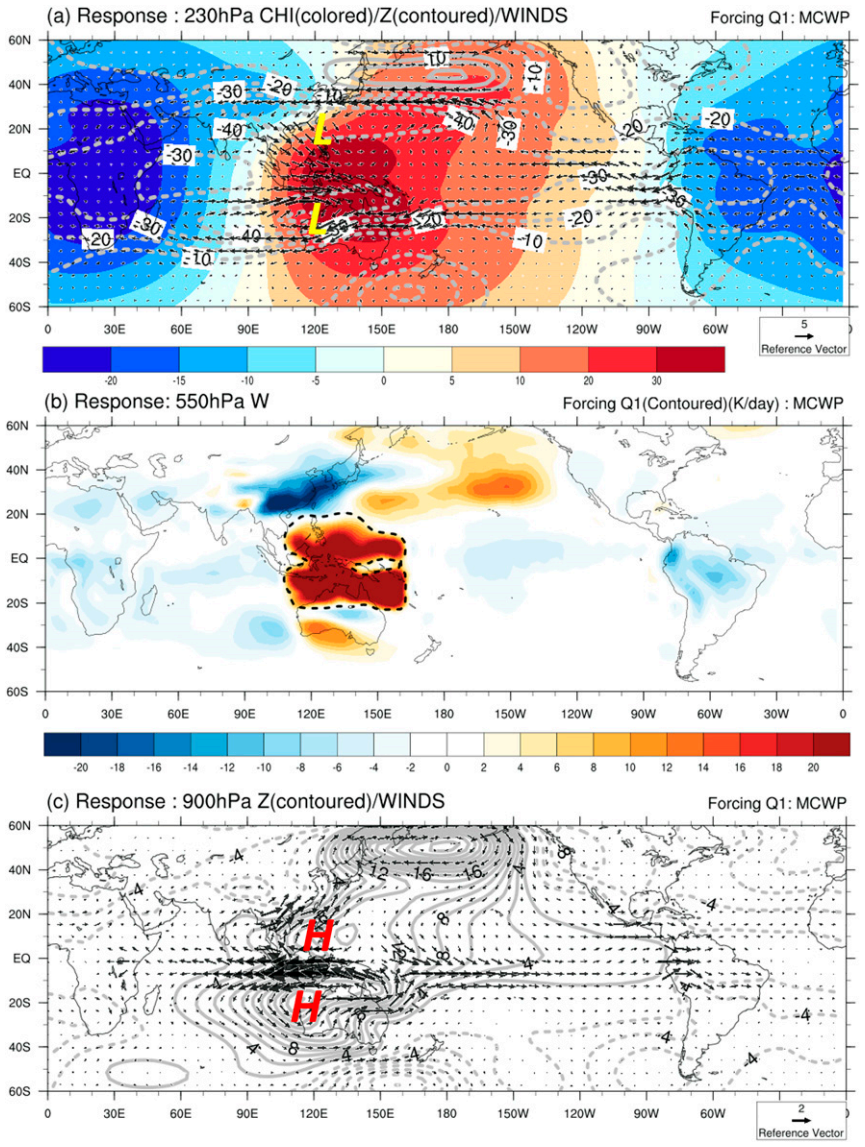

FIG. 14. As in Fig. 13, but for MCWP.

and extratropical responses in the East Asian jet region (EAJ). Here EAJ includes East Asia and western North Pacific. The wave signals are the pairs of positive (negative) height anomalies or anticyclonic (cyclonic) circulation associated with the MJO cooling (heating) in the lower troposphere and the pairs of reversed circulation in the upper troposphere as labeled by letters H and L for high and low centers in Figs. 13a,c, 14a,c, and 15a,c.

The extratropical responses in EAJ in the three experiments all show a similar meridional overturning circulation between MCWP and EAJ consisting of anomalous anticyclonic flow (positive height) over SCS–WP and the associated southwesterly winds from Indo-China through Taiwan to Japan in the lower troposphere (Figs. 13c, 14c, 15c) and reversed flow in the upper troposphere (Figs. 13a, 14a, 15a). Also notable in the extratropical responses in EAJ are the anomalous high in the northern Pacific centered at 45°N, 180° and the anomalous low in mainland China through the troposphere. This anomalous MCWP–EAJ teleconnection implies a weakened East Asian winter monsoon circulation system consisting of the Mongolian high, Aleutian low, East Asian jet, and northeasterly wind. The East Asian monsoon and MCWP convection are known to be closely coupled with each other (Chang and Lau 1982; Chang et al. 2005). In this study, we show such a coupled variability associated with the MJO convection in MCWP. The weakened winter monsoon develops along with ascending motion in midtroposphere extending from southeast China to Japan (Figs. 13b, 14b, 15b). The ascending motion is resulted primarily from a strong advection of vorticity of the mean zonal jet ($-\partial^2\overline{u}/\partial^2 y$) by the meridional thermal wind ($\partial v'/\partial p$) as required in quasigeostrophic theory (Kim et al. 2006).

The LBM results support our interpretation of the observational analysis of the influence of the MJO induced cooling

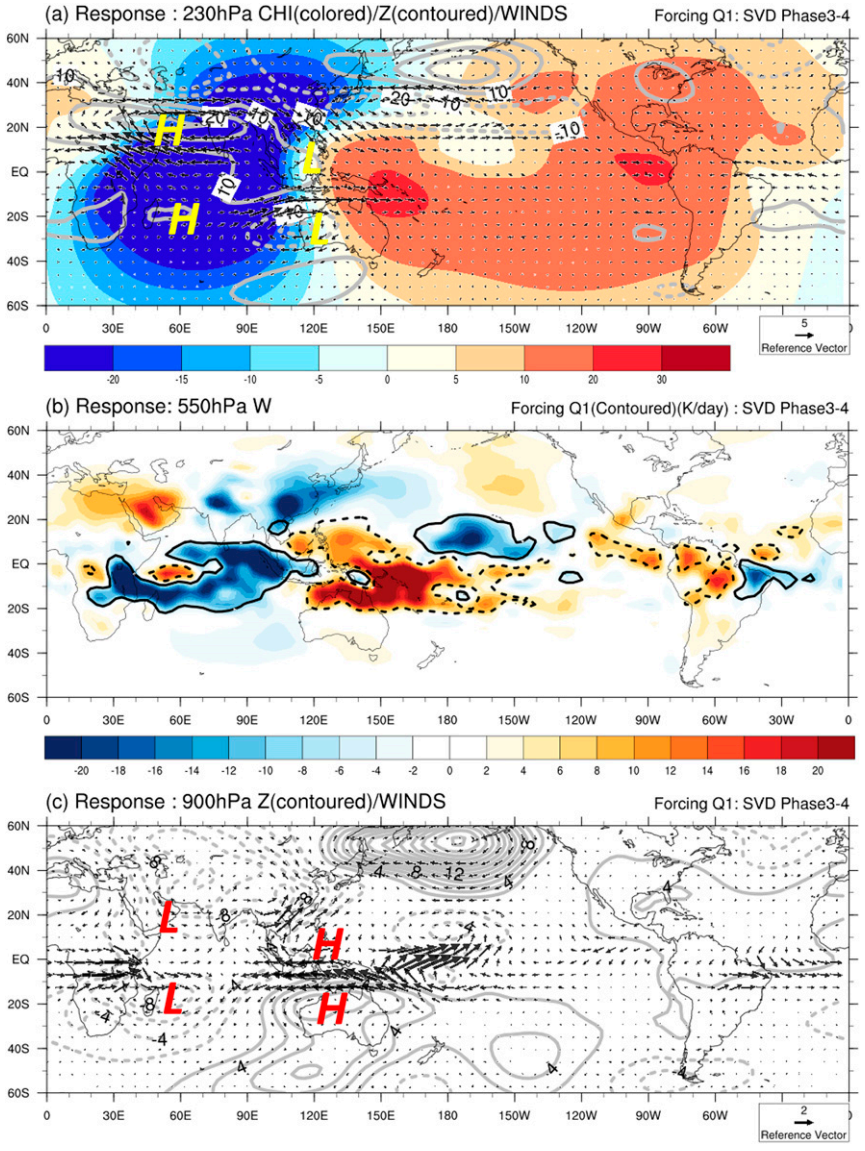

FIG. 15. As in Fig. 13, but for SVD34.

in MCWP on EA rainfall discussed in section 3c; that is, the MCWP cooling weakens the meridional overturning in East Asian winter monsoon, and the resultant ascending motion along with the meridional moisture advection in EA all contribute to enhanced rainfall. The model results further suggest that the MCWP cooling induced weakened meridional overturning circulation is a more direct cause of enhanced rainfall in EA than the IO heating (or the IO–MCWP heating dipole) induced Rossby wave teleconnection.

5. Summary and concluding remarks

Studies of the MJO influences on extratropical regions need to analyze meridional interactions. The commonly used real-time multivariate MJO (RMM) analysis of WH04 is based on a one-dimensional index, because variables to define the index are averaged latitudinally over the global tropical belt of 15°S–15°N. In this study we performed an SVD analysis to define a two-dimensional index to see if this may better describe the MJO phase structure in isolating the MJO influences on East Asian wintertime rainfall. In the SVD analysis we used the same OLR and U850 and U200 data during 37 boreal winter seasons of December–March as in the RMM analysis, except the wind data in the SVD domain are expanded to 30°N. The tropical convection parameter represented by the OLR in the two analyses are identical.

The two leading modes of the SVD analysis and the corresponding PCs are used to define eight phases of the MJO. The results show that

- SVD identifies the suppressed convection over the subtropical western North Pacific (Fig. 2f) as a critical signal that is out of phase with the East Asian rainfall; and

- the SVD composite of the evolution of EA rainfall anomalies shows a more conspicuous and coherent variation through the eight MJO phases, while the RMM composite is more ambiguous.

The SVD reveals that the EA winter rainfall starts in RMM P8, when convection over the Maritime Continent–western Pacific region is suppressed. This starting time is earlier than RMM phases P2–P3, which is characterized by active convection in the IO as identified by previous studies of MJO–EA winter rainfall relationship. Thus, it is possible that two mechanisms are operating: a response to the MCWP dominated heating and another response to the IO dominated heating. The occurrence of the MCWP cooling development leads that of the IO heating by at least one-eighth of a cycle.

To verify the observational results and examine the mechanism involved, we carry out numerical experiments using a global baroclinic model linearized about the winter mean states to simulate forced responses to imposed MJO heating. The model results show that enhanced EA rainfall starts in the phase of suppressed convection over the Maritime Continent–western Pacific region, earlier than the phase of Indian Ocean convection. This suppressed convection and related low-level divergence interact with the East Asian jet, which leads to an overall weakened East Asian monsoon system. The associated anomalous overturning circulation and low-level horizontal moisture convergence are the mechanism for the enhanced rainfall in EA. Thus, the MCWP cooling induced anomalous meridional circulation is a more direct cause of enhanced EA rainfall than the IO heating (or the IO–MCWP heating dipole) induced Rossby wave teleconnection.

Acknowledgments. This study is supported by the Ministry of Science and Technology, Taiwan, Grants MOST 109-2111-M-002-004 and MOST 109-2119-M-001-011. We thank Dr. Watanabe and Dr. Hayashi for the use of their model in this research.

Data availability statement. The observation and reanalysis data sets were downloaded from the following sources: Global Precipitation Climatology Project (GPCP) merged analysis of pentad precipitation (1979–2016; https://ftp.cpc.ncep.noaa.gov/precip/GPCP_PEN/; last accessed 2 January 2019); NOAA CDR OLR (1979–2016; https://www.ncei.noaa.gov/data/outgoing-longwave-radiation-daily/access/; Lee and NOAA CDR Program 2011; last accessed 24 March 2019); and NCEP–DOE atmospheric reanalysis (1979–2016; ftp://ftp.cdc.noaa.gov/Datasets/ncep.reanalysis2.dailyavgs/pressure/; last accessed 2 January 2019). The linear baroclinic model was downloaded from https://ccsr.aori.u-tokyo.ac.jp/~lbm/sub/lbm.html.

REFERENCES

Chang, C.-P., and K.-M. Lau, 1982: Short-term planetary-scale interactions over the tropics and midlatitude during northern winter. Part I: Contrasts between active and inactive periods. *Mon. Wea. Rev.*, **110**, 933–946, https://doi.org/10.1175/1520-0493(1982)110<0933:STPSIO>2.0.CO;2.

——, P. A. Harr, and H. J. Chen, 2005: Synoptic disturbances over the equatorial South China Sea and western Maritime Continent during boreal winter. *Mon. Wea. Rev.*, **133**, 489–503, https://doi.org/10.1175/MWR-2868.1.

Dee, D. P., and Coauthors, 2011: The ERA-Interim reanalysis: Configuration and performance of the data assimilation system. *Quart. J. Roy. Meteor. Soc.*, **137**, 553–597, https://doi.org/10.1002/qj.828.

Ferranti, L., T. N. Palmer, F. Molteni, and E. Klinker, 1990: Tropical–extratropical interaction associated with the 30–60 day oscillation and its impact on medium and extended range prediction. *J. Atmos. Sci.*, **47**, 2177–2199, https://doi.org/10.1175/1520-0469(1990)047<2177:TEIAWT>2.0.CO;2.

He, J., H. Lin, and Z. Wu, 2011: Another look at influences of the Madden–Julian Oscillation on the wintertime East Asian weather. *J. Geophys. Res.*, **116**, D03109, https://doi.org/10.1029/2010JD014787.

Hoskins, B. J., and D. J. Karoly, 1981: The steady linear response of a spherical atmosphere to thermal and orographic forcing. *J. Atmos. Sci.*, **38**, 1179–1196, https://doi.org/10.1175/1520-0469(1981)038<1179:TSLROA>2.0.CO;2.

——, and T. Ambrizzi, 1993: Rossby wave propagation on a realistic longitudinally varying flow. *J. Atmos. Sci.*, **50**, 1661–1671, https://doi.org/10.1175/1520-0469(1993)050<1661:RWPOAR>2.0.CO;2.

Hsu, P.-C., and T. Li, 2012: Role of the boundary layer moisture asymmetry in causing the eastward propagation of the Madden–Julian oscillation. *J. Climate*, **25**, 4914–4931, https://doi.org/10.1175/JCLI-D-11-00310.1.

Hung, C.-S., and C.-H. Sui, 2018: A diagnostic study of the evolution of the MJO maintained by wave dynamics, moistening, and convective-radiative processes. *J. Climate*, **31**, 4095–4115, https://doi.org/10.1175/JCLI-D-17-0139.1.

Hung, C.-W., H.-J. Lin, and H.-H. Hsu, 2014: Madden–Julian oscillation and the winter rainfall in Taiwan. *J. Climate*, **27**, 4521–4530, https://doi.org/10.1175/JCLI-D-13-00435.1.

Jeong, J.-H., C.-H. Ho, B.-M. Kim, and W.-T. Kwon, 2005: Influence of the Madden–Julian oscillation on wintertime surface air temperature and cold surges in East Asia. *J. Geophys. Res.*, **110**, D11104, https://doi.org/10.1029/2004JD005408.

——, B.-M. Kim, C.-H. Ho, and Y.-H. Noh, 2008: Systematic variation in wintertime precipitation in East Asia by MJO-induced extratropical vertical motion. *J. Climate*, **21**, 788–801, https://doi.org/10.1175/2007JCLI1801.1.

Jia, X., L. Chen, F. Ren, and C. Li, 2011: Impacts of the MJO on winter rainfall and circulation in China. *Adv. Atmos. Sci.*, **28**, 521–533, https://doi.org/10.1007/s00376-010-9118-z.

Jin, F.-F., and B. Hoskins, 1995: The direct response to tropical heating in a baroclinic atmosphere. *J. Atmos. Sci.*, **52**, 307–319, https://doi.org/10.1175/1520-0469(1995)052<0307:TDRTTH>2.0.CO;2.

Kanamitsu, M., W. Ebisuzaki, J. Woollen, S.-K. Yang, J. J. Hnilo, M. Fiorino, and G. L. Potter, 2002: NCEP–DOE AMIP-II Reanalysis (R-2). *Bull. Amer. Meteor. Soc.*, **83**, 1631–1643, https://doi.org/10.1175/BAMS-83-11-1631.

Kikuchi, K., B. Wang, and Y. Kajikawa, 2012: Bimodal representation of the tropical intraseasonal oscillation. *Climate Dyn.*, **38**, 1989–2000, https://doi.org/10.1007/s00382-011-1159-1.

Kiladis, G. N., J. Dias, K. H. Straub, M. C. Wheeler, S. N. Tulich, K. Kikuchi, K. M. Weickmann, and M. J. Ventrice, 2014: A comparison of OLR and circulation-based indices for tracking the MJO. *Mon. Wea. Rev.*, **142**, 1697–1715, https://doi.org/10.1175/MWR-D-13-00301.1.

Kim, B.-M., G.-H. Lim, and K.-Y. Kim, 2006: A new look at the midlatitude–MJO teleconnection in the Northern Hemisphere

winter. *Quart. J. Roy. Meteor. Soc.*, **132**, 485–503, https://doi.org/10.1256/qj.04.87.

Kim, D., J.-S. Kug, and A. H. Sobel, 2014: Propagating versus nonpropagating Madden–Julian oscillation events. *J. Climate*, **27**, 111–125, https://doi.org/10.1175/JCLI-D-13-00084.1.

Lee, H.-T., and NOAA CDR Program, 2011: NOAA Climate Data Record (CDR) of Daily Outgoing Longwave Radiation (OLR), version 1.2. NOAA National Climatic Data Center, accessed 24 March 2019, https://doi.org/10.7289/V5SJ1HH2.

Li, T., J. Ling, and P.-C. Hsu, 2020: Madden–Julian Oscillation: Its discovery, dynamics, and impact on East Asia. *J. Meteor. Res.*, **34**, 20–42, https://doi.org/10.1007/s13351-020-9153-3.

Li, W., P.-C. Hsu, J. He, Z. Zhu, and W. Zhang, 2016: Extended-range forecast of spring rainfall in southern China based on the Madden–Julian Oscillation. *Meteor. Atmos. Phys.*, **128**, 331–345, https://doi.org/10.1007/s00703-015-0418-9.

Lim, H., and C.-P. Chang, 1986: Generation of internal- and exernal-mode motions from internal heating: Effects of vertical shear and damping. *J. Atmos. Sci.*, **43**, 948–957, https://doi.org/10.1175/1520-0469(1986)043<0948:GOIAEM>2.0.CO;2.

Lin, H., G. Brunet, and J. Derome, 2009: An observed connection between the North Atlantic oscillation and the Madden–Julian oscillation. *J. Climate*, **22**, 364–380, https://doi.org/10.1175/2008JCLI2515.1.

Liu, Y., and P.-C. Hsu, 2019: Long-term changes in wintertime persistent heavy rainfall over southern China contributed by the Madden–Julian Oscillation. *Atmos. Oceanic Sci. Lett.*, **12**, 361–368, https://doi.org/10.1080/16742834.2019.1639471.

Matthews, A. J., 2008: Primary and successive events in the Madden–Julian Oscillation. *Quart. J. Roy. Meteor. Soc.*, **134**, 439–453, https://doi.org/10.1002/qj.224.

——, B. J. Hoskins, and M. Masutani, 2004: The global response to tropical heating in the Madden–Julian Oscillation during northern winter. *Quart. J. Roy. Meteor. Soc.*, **130**, 1991–2011, https://doi.org/10.1256/qj.02.123.

Mori, M., and M. Watanabe, 2008: The growth and triggering mechanisms of the PNA: A MJO–PNA coherence. *J. Meteor. Soc. Japan*, **86**, 213–236, https://doi.org/10.2151/jmsj.86.213.

Sardeshmukh, P. D., and B. J. Hoskins, 1988: On the generation of global rotational flow by steady idealized tropical divergence. *J. Atmos. Sci.*, **45**, 1228–1251, https://doi.org/10.1175/1520-0469(1988)045<1228:TGOGRF>2.0.CO;2.

Schreck, C. J., H.-T. Lee, and K. R. Knapp, 2018: HIRS outgoing longwave radiation—daily climate data record: Application toward identifying tropical subseasonal variability. *Remote Sens.*, **10**, 1325, https://doi.org/10.3390/rs10091325.

Seo, K.-H., and S.-W. Son, 2012: The global atmospheric circulation response to tropical diabatic heating associated with the Madden–Julian oscillation during northern winter. *J. Atmos. Sci.*, **69**, 79–96, https://doi.org/10.1175/2011JAS3686.1.

——, and H.-J. Lee, 2017: Mechanisms for a PNA-like teleconnection pattern in response to the MJO. *J. Atmos. Sci.*, **74**, 1767–1781, https://doi.org/10.1175/JAS-D-16-0343.1.

Straub, K. H., 2013: MJO initiation in the real-time multivariate MJO index. *J. Climate*, **26**, 1130–1151, https://doi.org/10.1175/JCLI-D-12-00074.1.

Tseng, K.-C., C.-H. Sui, and T. Li, 2015: Moistening processes for Madden–Julian oscillations during DYNAMO/CINDY. *J. Climate*, **28**, 3041–3058, https://doi.org/10.1175/JCLI-D-14-00416.1.

——, E. D. Maloney, and E. A. Barnes, 2018: Explaining the consistency of MJO teleconnection patterns with linear Rossby wave theory. *J. Climate*, **32**, 531–548, https://doi.org/10.1175/JCLI-D-18-0211.1.

——, ——, and ——, 2019: The consistency of MJO teleconnection patterns: An explanation using linear Rossby wave theory. *J. Climate*, **32**, 531–548, https://doi.org/10.1175/JCLI-D-18-0211.1.

Wang, B., and X. Xie, 1996: Low-frequency equatorial waves in vertically shears zonal flow. Part I: Stable waves. *J. Atmos. Sci.*, **53**, 449–467, https://doi.org/10.1175/1520-0469(1996)053<0449:LFEWIV>2.0.CO;2.

Watanabe, M., and M. Kimoto, 2000: Atmosphere–ocean thermal coupling in the North Atlantic: A positive feedback. *Quart. J. Roy. Meteor. Soc.*, **126**, 3343–3369, https://doi.org/10.1002/qj.49712657017.

Wheeler, M. C., and H. H. Hendon, 2004: An all-season real-time multivariate MJO index: Development of an index for monitoring and prediction. *Mon. Wea. Rev.*, **132**, 1917–1932, https://doi.org/10.1175/1520-0493(2004)132<1917:AARMMI>2.0.CO;2.

Xie, P., J. E. Janowiak, P. A. Arkin, R. Adler, A. Gruber, R. Ferraro, G. J. Huffman, and S. Curtis, 2003: GPCP pentad precipitation analyses: An experimental data set based on gauge observations and satellite estimates. *J. Climate*, **16**, 2197–2214, https://doi.org/10.1175/2769.1.

Xie, X., and B. Wang, 1996: Low-frequency equatorial waves in vertically shears zonal flow. Part II: Unstable waves. *J. Atmos. Sci.*, **53**, 3589–3605, https://doi.org/10.1175/1520-0469(1996)053<3589:LFEWIV>2.0.CO;2.

Yanai, M., S. Esbensen, and J.-H. Chu, 1973: Determination of bulk properties of tropical cloud clusters from large-scale heat and moisture budgets. *J. Atmos. Sci.*, **30**, 611–627, https://doi.org/10.1175/1520-0469(1973)030<0611:DOBPOT>2.0.CO;2.

Zhao, C., T. Li, and T. Zhou, 2013: Precursor signals and processes associated with MJO initiation over the tropical Indian Ocean. *J. Climate*, **26**, 291–307, https://doi.org/10.1175/JCLI-D-12-00113.1.